A first-order phase transition in Blatter's radical at high pressure

A First Order Phase Transition in Blatter's Radical at High Pressure

Authors

Edward T. Broadhurst[a], Cameron J. G. Wilson[a], Georgia A. Zissimou[b], Fabio Nudelman[a], Christos P. Constantinides[c], Panayiotis A. Koutentis[b] and Simon Parsons[a]*

[a]EaStCHEM School of Chemistry and Centre for Science at Extreme Conditions, The University of Edinburgh, King's Buildings, West Mains Road, Edinburgh, EH9 3FJ, Scotland

[b]Department of Chemistry, University of Cyprus, P.O. Box 20537, 1678 Nicosia, Cyprus

[c]Department of Natural Sciences, University of Michigan-Dearborn, 4914 Evergreen Road, Dearborn, Michigan, 48128-1491, USA

Correspondence email: s.parsons@ed.ac.uk

Funding information Engineering and Physical Sciences Research Council (grant No. EP-M506515-1 to Edward T. Broadhurst, Cameron J. G. Wilson; grant No. EP/R042845/1 to Simon Parsons); University of Michigan-Dearborn (award to Christos P. Constantinides); Cyprus Research Promotion Foundation (award to Panayiotis A. Koutentis); The University of Edinburgh (award to Edward T. Broadhurst, Cameron J. G. Wilson); Cambridge Crystallographic Data Centre (grant to Cameron J. G. Wilson); The State Laboratory (Cyprus) (gift to Panayiotis A. Koutentis); The Agricultural Research Institue (Cyprus) (gift to Panayiotis A. Koutentis); The Ministry of Agriculture (Cyprus) (gift to Panayiotis A. Koutentis); MedoChemie Ltd; Medisell Ltd.; Biotronics Ltd (gift to Panayiotis A. Koutentis); A.G. Leventis Foundation (grant to University of Cyprus).

Synopsis

The intramolecular conformational response to the build-up of compressed intermolecular interactions in Blatter's radical (1,3-diphenyl-1,4-dihydrobenzo[*e*][1,2,4]triazin-4-yl) induces a second order premonitory phase transition and then a first order phase transition above 5.34 GPa.

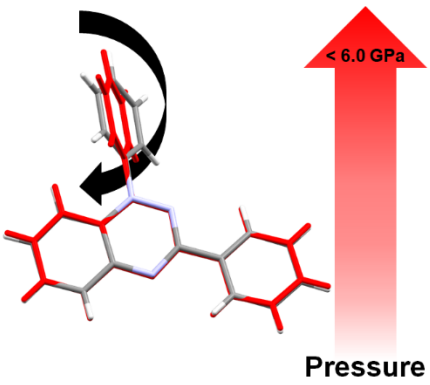

Abstract The crystal structure of Blatter's radical (1,3-diphenyl-1,4-dihydrobenzo[*e*][1,2,4]triazin-4-yl) has been investigated between ambient pressure and 6.07 GPa. The sample remains in a compressed form of the ambient pressure phase up to 5.34 GPa, the largest direction of strain being

parallel to direction of π-stacking interactions. The bulk modulus is 7.4(6) GPa, with a pressure derivative equal to 9.33(11). As pressure increases, the phenyl groups attached to the N1 and C3 positions of the triazinyl moieties of neighbouring pairs of molecules approach each other, causing the former to begin to rotate between 3.42 to 5.34 GPa. The onset of the phenyl rotation may be interpreted as a second order phase transition which introduces a new mode for accommodating pressure. It is premonitory to a first order, isosymmetric phase transition which occurs on increasing pressure from 5.34 to 5.54 GPa. Although the phase transition is driven by volume minimisation, rather than relief of unfavourable contacts, it is accompanied by a sharp jump in the orientation of the rotation angle of the phenyl group. DFT calculations suggest that the adoption of a more planar conformation by the triazinyl moiety at the phase transition is owed to relief of intramolecular H···H contacts at the transition. Although no dimerization of the radicals occurs, the π-stacking interactions are compressed by 0.341(3) Å between ambient pressure and 6.07 GPa.

Keywords: High pressure; π-stacking; Organic radicals; Intermolecular interactions; Phase transitions

1. Introduction

Blatter's radical, 1,3-diphenyl-1,4-dihydrobenzo[*e*][1,2,4]triazin-4-yl (**1**), was first prepared by (Blatter & Lukaszewski, 1968). It is stable to air and moisture and in common with other Blatter-type radicals (Gallagher *et al.*, 2016), can be sublimed without degradation (Hande *et al.*, 2020). The stability of radical **1** is partly attributed to delocalization of the unpaired electron over the π system and can be influenced by substituents on the aromatic rings. For example, addition of a 7-trifluoromethyl group on the benzotriazinyl moiety at the 7-position blocks oxidation and can make it "super" stable towards oxidation (Constantinides, Koutentis, Krassos*, et al.*, 2011). Stability can also be altered through steric hindrance by substituents at the N1 position, which also affects the planarity of the molecule (Kaszyński *et al.*, 2016). These physical properties inspired extensive research into developing new syntheses to increase the structural diversity of Blatter-type radicals as functional materials (Koutentis & Lo Re, 2010, Constantinides, Koutentis & Loizou, 2011, Berezin *et al.*, 2012, Berezin *et al.*, 2013, Constantinides, Berezin, Manoli*, et al.*, 2014, Kaszyński *et al.*, 2016, Savva *et al.*, 2017, Bartos *et al.*, 2020). Recent reviews of the synthesis and properties of Blatter-type radicals are available (Constantinides & Koutentis, 2016, Ji *et al.*, 2020, Rogers *et al.*, 2020).

Thiazyls, phenalenyls and triazinyls (of which **1** is an example) are classes of bistable organic radicals which change between different magnetic or charge carrier states in response to external stimuli, such as variation of temperature, as a result of the ordering or disordering of the unpaired spins throughout the crystal structure. The way in which these responses are influenced by structure is usually investigated by comparing the properties of different chemical derivatives, but the application of pressure is also a powerful method for revealing structure-property relationships (Katrusiak, 2019,

Zakharov & Boldyreva, 2019, Moggach & Oswald, 2020). High-pressure studies of metal organic frameworks have, for example, revealed gating mechanisms for guest uptake (McKellar & Moggach, 2015). Other studies have be applied to investigate magneto-structural correlations in molecule-based magnets containing transition metals (Etcheverry-Berrios *et al.*, 2020) and to spin crossover complexes (Halcrow, 2007, Guionneau & Collet, 2013, Gaspar *et al.*, 2018). In the field of molecular magnets based on *p*-block elements, Oakley and co-workers have investigated the response of sulfur- and selenium-based heterocyclic radicals to pressure. Benzoquino-bis-1,2,3-dithiazole, which displays a small band gap at ambient conditions, undergoes an insulator to semiconductor transition above 8.0 GPa (Mailman *et al.*, 2017), while bisdiselenazolyl radicals undergo a transition from an insulating state to one displaying weakly metallic behaviour beyond 7 GPa (Leitch *et al.*, 2011).

Herein, we investigated the effect of pressure on Blatter's radical **1**. While dimerization of the radical is possible, this is rare and has only been reported once for a Blatter-type radical (Berezin *et al.*, 2015). Instead, we explored the extent to which pressure can influence the intra- and inter- molecular geometry. While bond distances and angles in organic crystals are relatively insensitive to pressure, both torsional and conformational geometry changes can occur. For example, the amino acid cysteine above 1.8 GPa undergoes a phase transition accompanied by a change in the NCCS torsion angle from *ca.* 60 to −60° (Moggach *et al.*, 2006). Pressure sensitivity in radical **1** can demonstrate that, as in the examples cited above, high pressure is an interesting means for determining structure-property relationships in this class of material.

2. Experimental

2.1. Single crystal X-ray diffraction

Crystals of Blatter's radical, 1,3-diphenyl-1,4-dihydrobenzo[*e*][1,2,4]triazin-4-yl (**1**), were prepared according to a literature procedure (Koutentis & Lo Re, 2010). Diffraction data were collected on a Bruker AXS D8 Venture diffractometer using Mo Kα radiation (λ = 0.71073 Å) at pressures up to 6.07 GPa in two loadings, the limits of each study being dictated by the quality of the diffraction pattern. Each crystal was loaded into a Merrill−Bassett diamond-anvil cell (DAC) with half opening angle of 38°, 600 μm Boehler−Almax-cut diamonds and tungsten carbide backing plates (Merrill & Bassett, 1974). A tungsten gasket of thickness 300 μm indented to 155 μm and hole diameter of 300 μm was used, along with a 4:1 mixture of methanol and ethanol as a pressure-transmitting medium (Klotz *et al.*, 2009). A small ruby chip was also included in the sample loading and the ruby fluorescence method was used to measure the pressure (Mao *et al.*, 1978).

Data were collected as in (Dawson *et al.*, 2004) and integrated using SAINT (Bruker, 2019). Corrections for the DAC shading, absorption and other systematic errors were applied using the multi-scan procedure in SADABS. The initial structure was solved using dual-space methods [SHELXT, (Sheldrick, 2015)], while high-pressure structures were refined using the atomic coordinates of the

structures from the preceding pressure points as starting models. Refinement was performed by full-matrix least-squares on $|F|^2$ (SHELXL) implemented in Olex2 (Sheldrick, 2015, Dolomanov *et al.*, 2009). Intramolecular bond distances and angles in all refinements against data collected at high pressure were restrained to those observed at ambient pressure. Where possible, non-hydrogen atoms were refined with anisotropic displacement parameters (adps) subject to enhanced rigid-bond restraints (Thorn *et al.*, 2012). In cases where an atom developed non-positive definite adps (though still positive definite within error), it was modelled isotropically. Hydrogen atoms were placed in calculated positions and constrained to ride on their parent atoms. Selected crystal and refinement data are listed below in Table 1, a complete table (Table S1) is available in the ESI.

2.2. Calculation of intermolecular interaction energies using the PIXEL method

Lattice energies and intermolecular interaction energies were calculated using the semi-empirical PIXEL method (Gavezzotti, 2005, 2007, 2011). PIXEL calculates energies by modelling each molecular component as a grid of small cubes ('pixels') of electron density. Interactions are calculated between a central reference molecule and other molecules within a cluster generated from the space group symmetry. Intermolecular energies are calculated from the sum of electrostatic, polarisation, dispersion and Pauli repulsion terms accumulated from each pixel–pixel combination in a dimer. The sum of all cluster interaction energies gives the lattice energy, calculated assuming that no modifications to the molecular structure occur on sublimation. In this study, the cluster radius was 14 Å, and the molecular electron densities were obtained in steps of 0.08 Å using DFT with the 6-31G** basis set and the B3LYP functional in Gaussian09 (Frisch *et al.*, 2009). The PIXEL calculations themselves were accomplished with the CLP-PIXEL suite using a condensation level of 4 (*i.e.* the original pixels from *Gaussian* were combined into 4 × 4 × 4 blocks of dimension 0.32 Å) using the MrPIXEL interface (Reeves *et al.*, 2020).

2.3. Other programs used

Structures were visualised in Mercury (Macrae *et al.*, 2020). The principal axes of strain were calculated using *PASCaL* (Cliffe & Goodwin, 2012). EoSFit7-GUI (Angel *et al.*, 2014) was used for equation of state (EoS) calculations. CrystalExplorer was used for Hirshfeld surface analysis (Spackman *et al.*, 2008, Spackman *et al.*, 2021). The volumes of the voids and the network of intermolecular contacts, that is the space enclosed within the van der Waals radii of all atoms (Alvarez, 2013), were calculated for each pressure point using the Monte-Carlo procedure CELLVOL (Wilson *et al.*, 2021).

Table 1 Selected experimental data collection and refinement information. A complete table is available in Table S1 in the ESI. For all structures: $C_{19}H_{14}N_3$, M_r = 284.33, monoclinic, $P2_1/n$, Z = 4. Experiments were carried out at 298 K with Mo $K\alpha$ radiation using a Bruker D8 Venture diffractometer. H-atom parameters were constrained.

Pressure (GPa)	0.00	2.53	3.42	5.34	5.54	6.07
Phase	I	I	I	I	II	II
Crystal data						
a, b, c (Å)	10.4887 (4), 6.9632 (2), 19.8755 (7)	10.1864 (8), 6.3323 (5), 19.118 (3)	10.1302 (4), 6.2215 (3), 18.9550 (18)	10.0326 (6), 6.0553 (4), 18.571 (3)	10.0002 (5), 6.0842 (3), 18.352 (2)	9.9663 (7), 6.0642 (4), 18.252 (3)
β (°)	99.441 (2)	99.822 (9)	99.899 (5)	100.029 (7)	100.026 (6)	100.025 (9)
V (Å^3)	1431.94 (9)	1215.1 (3)	1176.85 (13)	1110.93 (19)	1099.55 (15)	1086.3 (2)
Data Collection						
No. of measured, independent and observed [$I > 2\sigma(I)$] reflections	8006, 2511, 1422	6204, 865, 558	5411, 805, 558	6150, 748, 537	4978, 734, 545	5236, 727, 481
R_{int}	0.044	0.050	0.035	0.043	0.032	0.057
Refinement						
$R[F^2 > 2\sigma(F^2)]$, $wR(F^2)$, S	0.057, 0.188, 1.06	0.043, 0.112, 1.05	0.036, 0.097, 1.03	0.037, 0.102, 1.09	0.033, 0.086, 1.08	0.050, 0.140, 1.00
Data Completeness	0.991	0.352	0.339	0.330	0.327	0.327

Computer programs: *SAINT* V8.40A (Bruker, 2019), *SHELXT* 2014/5 (Sheldrick, 2014), XL (Sheldrick, 2008), Olex2 1.3 (Dolomanov *et al.*, 2009).

3. Results and Discussion

3.1. Ambient pressure structure

1,3-Diphenyl-1,4-dihydrobenzo[*e*][1,2,4]triazin-4-yl (**1**, Figure 1a) crystallizes in the space group $P2_1/n$. The crystallographic atom numbering scheme, shown in Figure 1b, taken from the recent paper by (Constantinides *et al.*, 2020), is used for the discussion below rather than IUPAC atom numbering. Radical **1** consists of a central benzo-1,2,4-triazinyl moiety with two phenyl substituents attached at N1 and C1. The triazinyl moiety is almost planar, with an angle of 3.66(2)° between the N1-N2-C1-N3 and N1-C3-C2-N3 fragments.

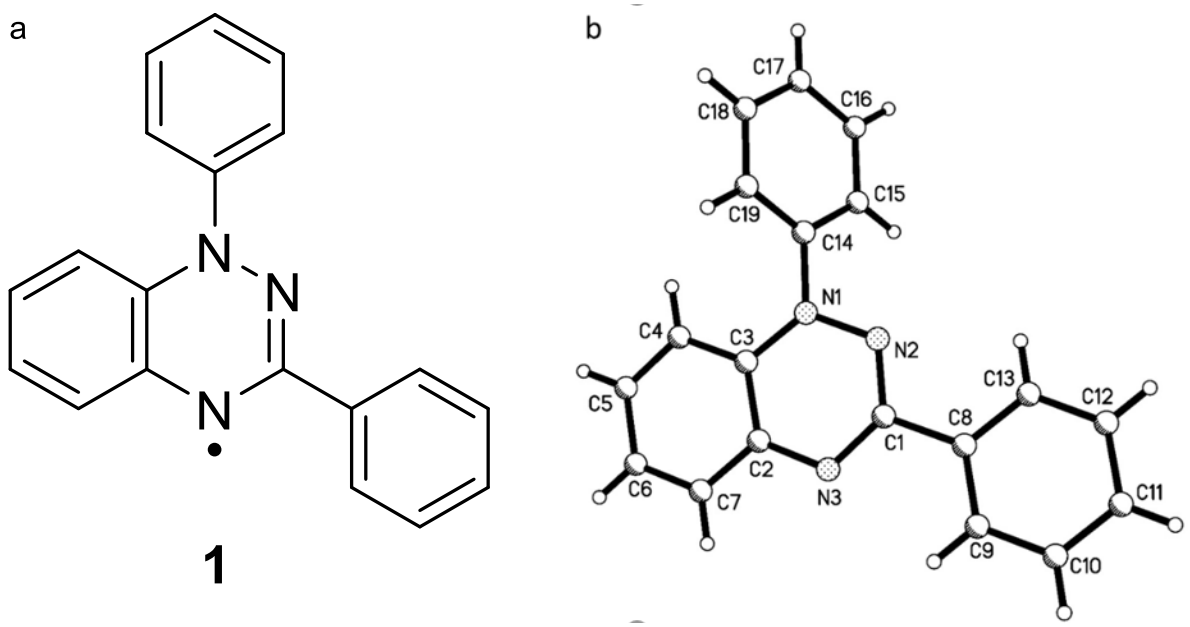

Figure 1 a) Structural formula of Blatter radical 1,3-diphenyl-1,4-dihydrobenzo[*e*][1,2,4]triazin-4-yl (**1**). b) Molecular structure at ambient pressure showing the atom-numbering scheme.

Intermolecular interactions, which are dominated by dispersion, were analysed using the PIXEL method (Tables 2 and S2). Symmetry-equivalent contacts (Table 2) are labelled A/A' *etc.*, and *mol2* format files depicting each contact individually are available in the ESI. There are 12 contacts in the first molecular coordination sphere, identified by their significant Pauli repulsion terms. Layers form in the *ac* planes in which each molecule is surrounded by six neighbours (contacts E-G') with three contacts each to molecules in the layers above (contacts A, B and C) and below (contacts A', B' and D) (Figure S1a). When viewed along the *b* axis, the contacts to the layers above and below are eclipsed, giving the structure a hexagonal close packed topology. Figure S1b depicts these interactions using energy frameworks imposed on a single molecule (Turner *et al.*, 2015, Mackenzie *et al.*, 2017).

Table 2 Intermolecular interaction energies in the first coordination sphere of **1** at ambient pressure. All energies are in kJ mol^{-1}. Operators for equivalent contacts are: A': ½−*x*, ½+*y*, 1.5−*z*; B': 1.5−*x*, −½+*y*, 1.5−*z* ; E': 1+*x*, *y*, *z*; F': −½+*x*, 1.5−*y*, ½+*z*; G': −½+*x*, 1.5−*y*, −½+*z*

Interaction label	Symmetry	Centroid distance (Å)	Coulombic	Polarisation	Dispersion	Repulsion	Total
A	½−*x*, −½+*y*, 1.5−*z*	5.846	−1.8	−6.3	−65.9	34.4	−39.6
B	1.5−*x*, ½+*y*, 1.5−*z*	7.717	−9.0	−2.7	−25.7	11.2	−26.3
C	1−*x*, 1−*y*, 1−*z*	8.387	−7.1	−2.9	−33.8	19.0	−24.8
D	1−*x*, 2−*y*, 1−*z*	8.980	−3.9	−1.5	−17.2	5.7	−16.8
E	1−*x*, *y*, *z*	10.489	−12.5	−5.8	−21.6	22.7	−17.3
F	½+*x*, 1.5−*y*, −½+*z*	11.996	−1.4	−1.6	−15.1	8.0	−10.1
G	½+*x*, 1.5−*y*, ½+*z*	10.474	−2.5	−1.4	−12.3	7.5	−8.8
H	−*x*, 1−*y*, 1−*z*	10.990	−2.0	−0.3	−6.2	1.2	−7.3
I	1−*x*, 1−*y*, 2−*z*	12.518	0.0	0.0	−2.1	0.2	−1.9

The strongest contacts are formed between layers. The strongest of all contacts (A and A') are π-stacking interactions between the benzotriazinyl and C-Ph substituent. The centroid-to-centroid distance between the triazinyl and the symmetry-generated C-Ph substituent is 3.6786(14) Å, that between C-Ph and the symmetry-generated triazinyl centroid is 3.5890(14) Å (Figure 2a). The angle between the triazinyl moiety and the symmetry-generated C-Ph substituent is 4.11(12)°. The next strongest contact (B and B') involves a pair of equivalent T-shaped π interactions between the N-Ph substituents (Figure 2b). The angle between the mean planes on the symmetry generated phenyl substituents (C14-C19) in this interaction is 75.65(15)° with a centroid-centroid distance equal to 5.0378(18) Å, close to optimal geometry for this type of interaction (Sinnokrot *et al.*, 2002). Contacts C and D are inequivalent as they are formed by inversion centres and are best described as general dispersion interactions, contact C being shorter and stronger than D.

Within the *ac* layers, the strongest two contacts are formed by lattice translations. Four others of similar energy are formed by two sets of glide operations. The interactions within the layers are also mostly of general dispersion type, but contacts E and E', which involve CH···N contacts, have a significant electrostatic contribution. There are, in addition, two long contacts (H and I) which are of marginal significance at ambient conditions, but with increasing pressure, become more important.

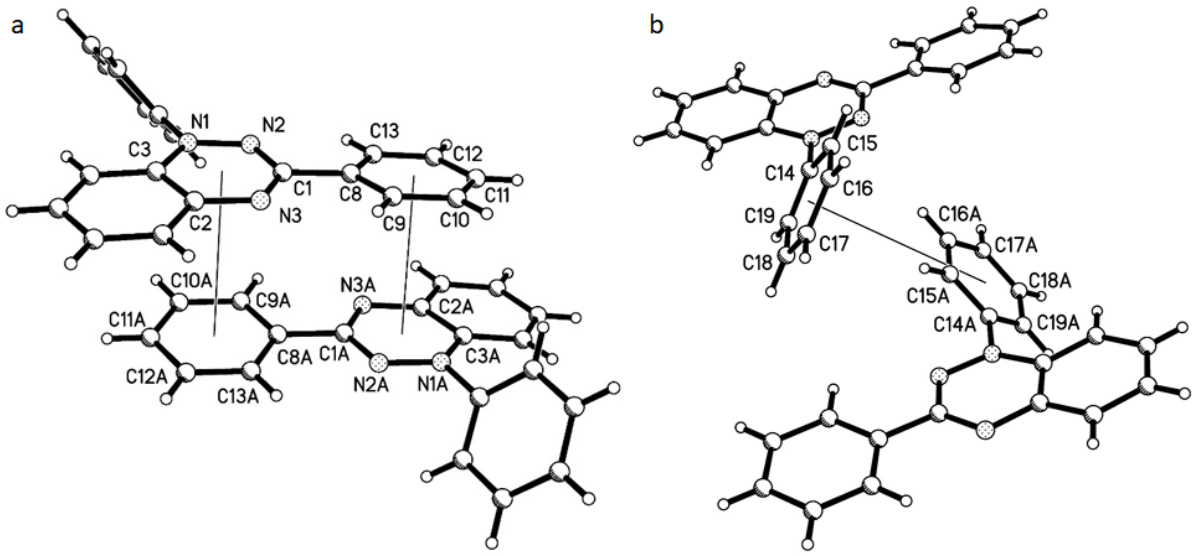

Figure 2 a) Formation of the strongest (π-stacking) interaction in the crystal structure of radical **1**. This is the interaction between the C-Ph group and the benzotriazinyl core (interaction A). b) Formation of the second strongest T-shaped π interaction in the crystal structure of radical **1** (interaction B).

3.2. Response of the lattice parameters to application of pressure

Compression of the crystal structure of radical **1** is anisotropic across the pressure range. Animations of the sample under increasing pressure viewed along *a, b* and *c* axes are available in the ESI. The

animations (that viewed along *a* is clearest) show that the N-Ph substituent begins to rotate above 3.42 GPa as the molecules involved in interaction F are displaced towards one another. The rotation becomes more substantial between 5.34 and 5.54 GPa, leading to a phase transition. We shall refer to the low- and high-pressure forms as phases I and II, respectively.

The relative changes in the unit cell parameters are shown in Figure 3a. The most compressible unit-cell axis is *b*, which shortens by 13%. This axis is aligned with the π-stacking interactions (A) between the *ac* layers of molecules. The *a* and *c* unit-cell axes shorten 5 and 9%. The phase transition causes discontinuities in all three unit-cell axes, with *a* and *c* decreasing in length, but *b* increasing.

The variation of the unit-cell volume of radical **1** with pressure is shown in Figure 3b; the discontinuity between 5.34 and 5.54 GPa indicates that the phase transition is first order. Prior to the transition, the volume reduces monotonically, and can be fitted ($\chi^2 = 1.44$) to a 3rd order Birch-Murnaghan equation of state (EoS) to give a bulk modulus (K_0) equal to 7.4(6) GPa, and a pressure derivative (K') equal to 9.33(11). These values are typical for molecular solids. There are not enough points to derive a reliable EoS for phase II.

Although the variation of the unit-cell dimensions yields a useful overview of the effects of pressure, the principal directions of the strain tensor are independent of the choice of unit cell and give a more objective characterisation of the anisotropy of compression. The eigenvalues and eigenvectors of the strain tensor are listed in Table 3 and shown graphically in Figure S2 (ESI). One axis of the strain tensor must lie along the *b* axis by symmetry, but the others may lie in any orthogonal directions in the *ac* plane.

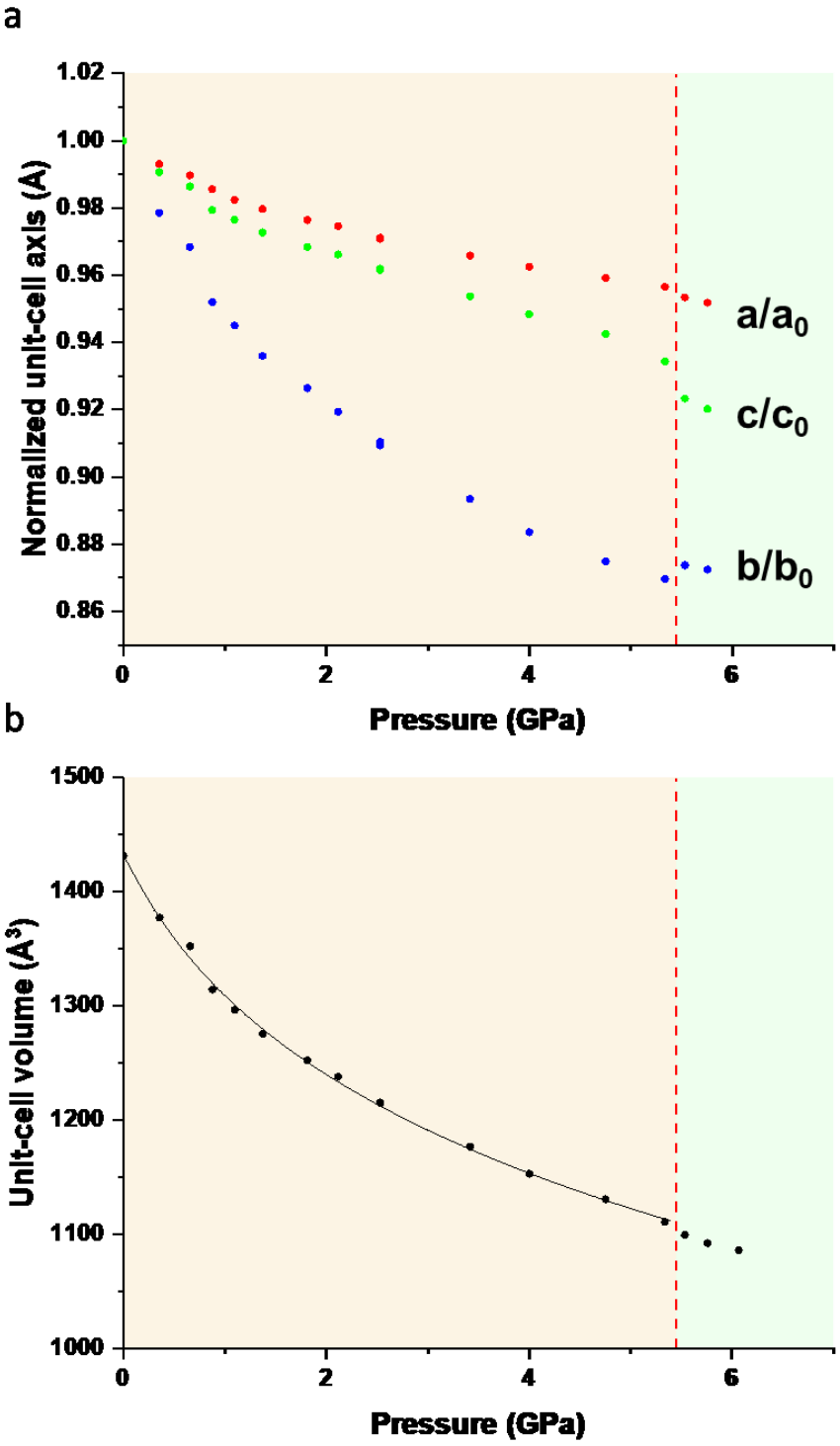

Figure 3 a) Normalized unit-cell axis lengths as a function of pressure. b) Pressure dependence of the unit-cell volume of radical 1 crystal. The line shows the fit to the 3rd order Birch-Murnaghan equation of state up to 5.34 GPa. Error bars lie within the symbols. The dashed vertical lines in parts (a) and (b) and in other figures mark the phase transition after 5.34 GPa.

Table 3 Principal axes of strain for the crystal structure of radical **1** over the pressure series.

Axis	Direction	Compressibility (TPa^{-1})
X_1	[010]	18.5(8)
X_2	[0.61 0 0.79]	12.2(5)
X_3	[0.99 0 −0.13]	7.2(2)

Consistent with the analysis of the cell dimensions given above, the most compressible direction (X_1) is [010] and the π-stacking interactions. The direction of smallest strain (X_3) makes an angle of 7.48° with **a**, which is also consistent with *a* being the least compressible along this axis. It aligns with the N-to-phenyl covalent bond and the CH···N contact formed in interaction E. X_2 is parallel to the direction of the displacement of the benzotriazinyl moiety towards the N-Ph substituent in interaction F, which drives the rotation and subsequent phase transition.

3.3. Lattice energy and enthalpy

The lattice energy of radical **1** with increasing pressure is shown in Figure S3 using data in Table S2. Over the pressure series, the lattice energy increases by 63.8 kJ mol^{-1} and passes through a minimum at 0.88 GPa (more negative than at ambient pressure by 9.5 kJ mol^{-1}). This has been observed previously in pressure studies of the OP polymorph of ROY (Funnell *et al.*, 2019) and *L*-serine (Wood *et al.*, 2008). Extrapolation of the phase I EoS through the phase transition to 5.54 GPa gives a volume of 1108(2) $Å^3$. The volume of phase-II observed at this pressure is 1099.55(15) $Å^3$. The more efficient packing in phase II contributes a pV stabilisation relative to phase I of −7.04 kJ mol^{-1} at 5.54 GPa. Extrapolation of the phase I lattice energy to 5.54 GPa yields values, depending on the method used, of between −79.5 and −82.3 kJ mol^{-1}, compared to −79.1 kJ mol^{-1} for phase II, suggesting that the lattice energy becomes slightly more positive over the phase transition, but that this is out-weighed by the pV term. The driving force of the transition is therefore likely to be volume minimisation rather than relief of strain built up in short contacts, as is often the case in other high-pressure phase transitions (Johnstone *et al.*, 2010, Cruz-Cabeza *et al.*, 2019).

3.4. Intermolecular interactions

PIXEL calculations were carried out at each pressure point and the energies of the intermolecular interactions in the first coordination sphere are shown as a function of centroid distance in Figure 4, with numerical data available in the ESI (Table S3). The curves in Figure 4 represent the regions of each intermolecular potential hypersurface which are sampled over the course of compression. The clear implication of the compression movie viewed along *a* is that the approach of the C-Ph substituent in one molecule begins to push on the N-Ph substituent of a neighbouring molecule, causing it to rotate, increasing the C3-N1-C14-C19 torsional angle (Figure 5) and the potentials of Figure 4 quantify the intermolecular energy changes that cause this rotation.

The largest energy changes are seen in the contacts between the layers (A-D). While contacts B-D are stabilised between ambient pressure and 1.10 GPa, contact A destabilises immediately on compression and shows the largest degree of destabilisation of all contacts between 0 and 6.07 GPa. It is pushed into a repulsive region of its potential above 5.34 GPa, just prior to the phase transition. The two π-stacking interactions which comprise contact A compress by 0.341(3) and 0.215(3) Å between ambient pressure and 6.07 GPa, reaching 3.338(3) and 3.374(3) Å. The sensitivity of π-stacking energies to pressure has been noted in other structures, for example 4-iodobenzonitrile (Giordano *et al.*, 2019). Above 1.10 GPa the energies of contacts B-D also begin to destabilise, all three becoming slightly longer at the phase transition. More discontinuous behaviour is seen in the intra-layer contacts (Figure 6). Interaction F is initially quite insensitive to pressure, but there is a sudden increase in the energy at 3.42 GPa, the point at which the N-Ph begins to rotate.

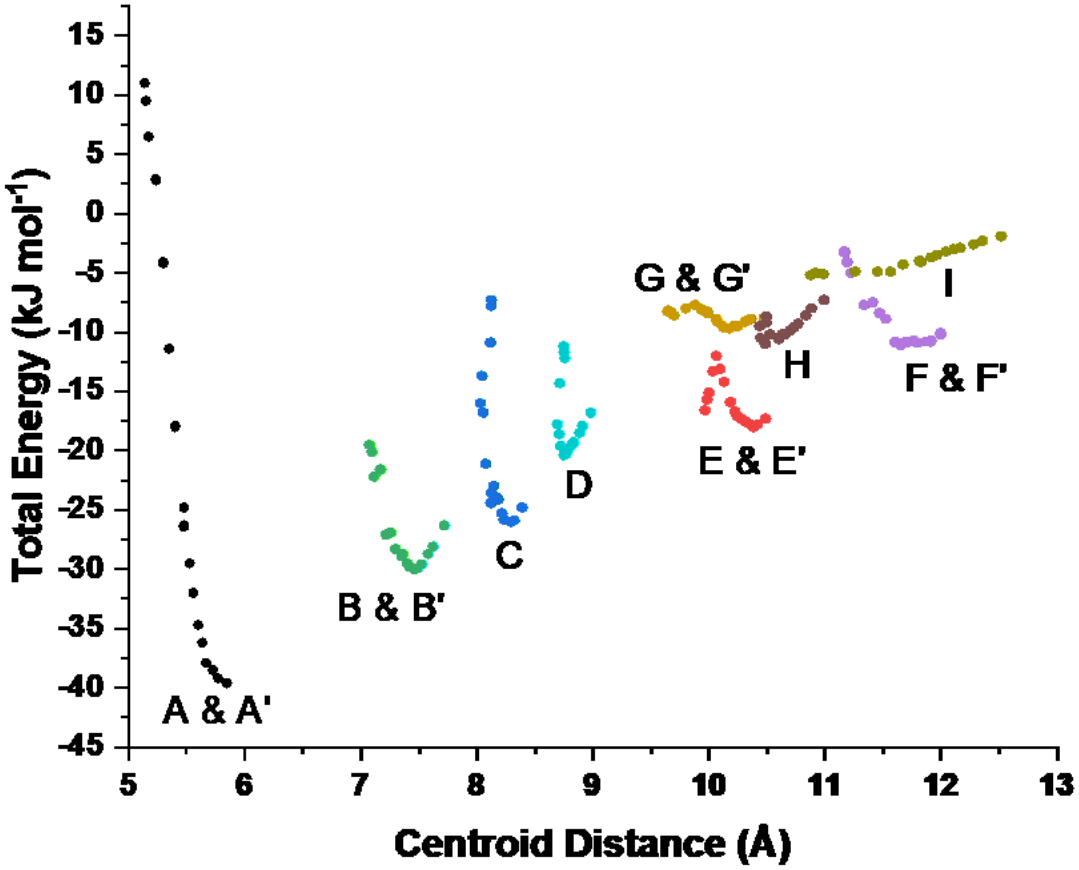

Figure 4 Plot of the intermolecular interactions in the first coordination sphere of radical **1** with centroid distance. Increasing pressure is from right to left.

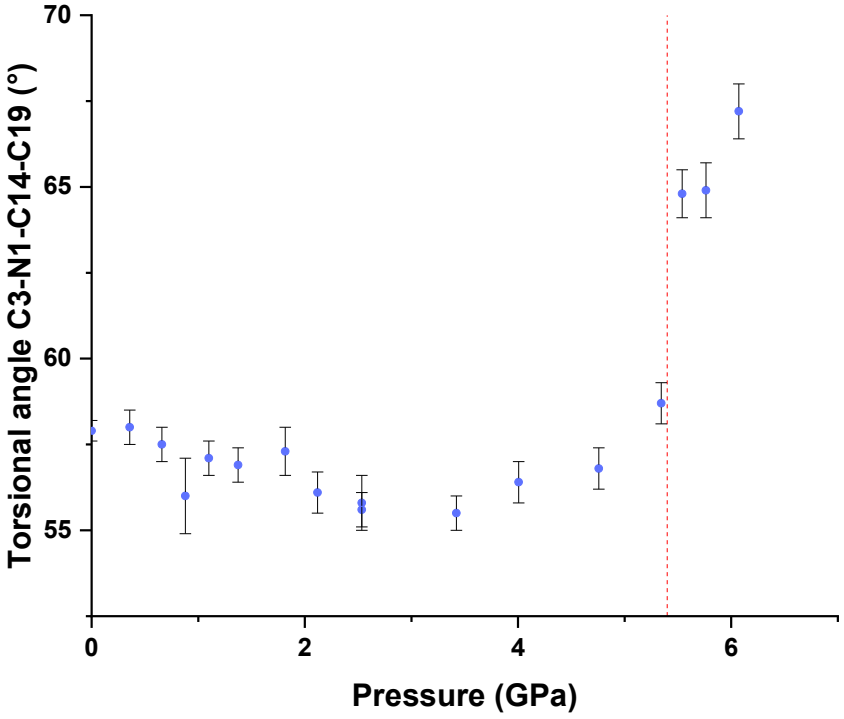

Figure 5 Plot of the N-Ph torsional angle with increasing pressure.

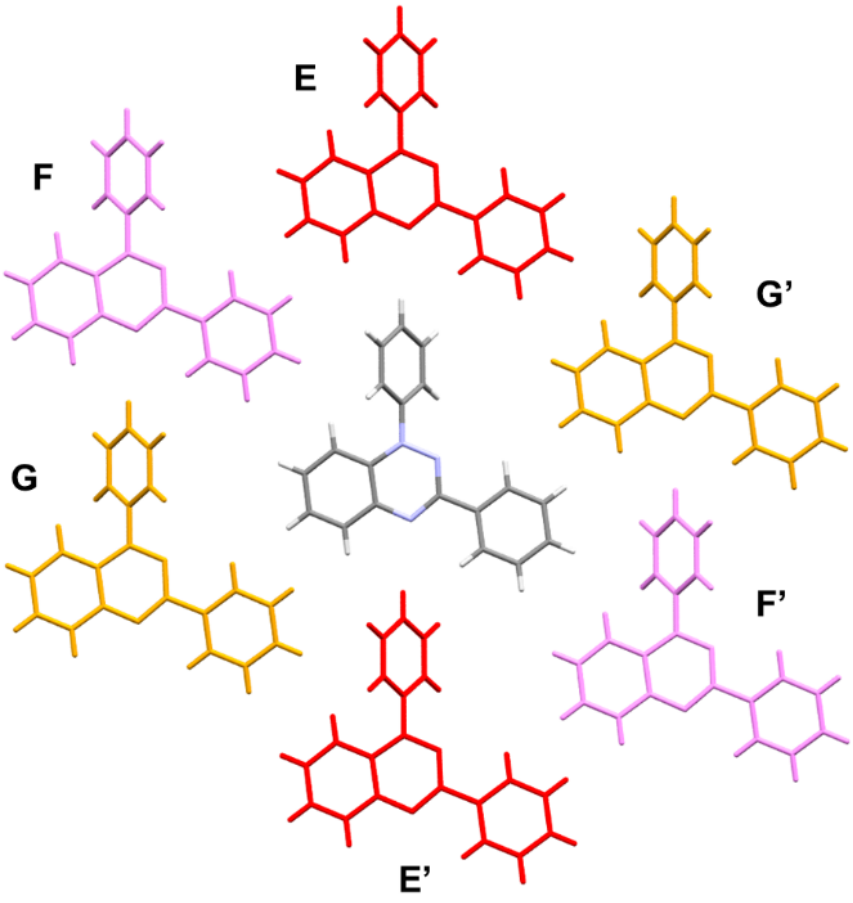

Figure 6 Molecules of radical **1** in the *ac* layers. Colours are as in Figure 4.

The phase transition corresponds to a jump in the N-Ph rotation angle, but the rotation begins prior to the transition in an example of premonitory behaviour. The data in Figure 4 quantify the effect of this 'push' and rotation in terms of energy, the difference between the energy at 2.53 and 3.42 GPa being just 2 kJ mol^{-1} (see Table S3). At the phase transition, the rotation of the N-Ph substituent relieves short C···H contacts which occur in interaction F as pressure increases (Figure S4). At ambient pressure the (un-normalised) C18···H11 and C19···H11 distances are 3.05 and 3.11 Å, respectively, but at 3.42 GPa they shorten to 2.69 and 2.68 Å, and at 5.24 GPa they both measure 2.58 Å. The sum of the van der Waals radii of C and H is 2.90 Å. C19···H11 lengthens after the transition to 2.61 Å at 5.54 GPa and the onset of greater rotation of the N-Ph group.

The rotation of the N-Ph substituent enables interaction E, which includes the short C17-H17···N3 contact, to shorten without incurring unfavourable H16···H9 and H18···H7 interactions. The energy of interaction E reaches a maximum at 4.75 GPa and begins to become more negative thereafter, the interaction having an energy at 6.07 GPa similar to that at ambient pressure.

The rotation of the N-Ph substituent also creates more space for shortening interaction G. As a result, the energy of interaction G is quite insensitive to pressure, so that reducing its length provides a means to accommodate pressure at almost no cost in terms of energy.

Contacts H and I, which are long-range dispersion contacts of marginal significance at ambient pressure, become more stabilising at high pressure reaching −8.7 and −5.2 kJ mol^{-1} at 6.07 GPa. The molecular coordination number therefore changes from 12 to 14 over the course of compression. The energy differences of interactions in the first coordination sphere at selected pressure points is shown in the ESI (Table S4).

3.5. The effect of pressure on intramolecular geometry

While the increase in pressure affects the N-Ph torsional angle significantly beyond 5.34 GPa, the effect on the C-Ph torsional angle is smaller, changing from −6.3(4) to −8.4(4)° (Figure S5). The involvement of the C-Ph group in the π-stacking interaction A likely limits the capacity for substantial changes in its orientation.

Further intramolecular effects occur within the triazinyl core, which becomes steadily more planar with pressure, the 'hinge' angle between the N1-N2-C1-N3 and N1-C3-C2-N3 planes decreasing steadily from 3.66(2)° at ambient pressure before levelling off at 2.08(3)° above 3 GPa. The angle then undergoes a sudden drop before the phase transition after 4.76 GPa (Figure 7), becoming 0.87(4)° at 6.07 GPa.

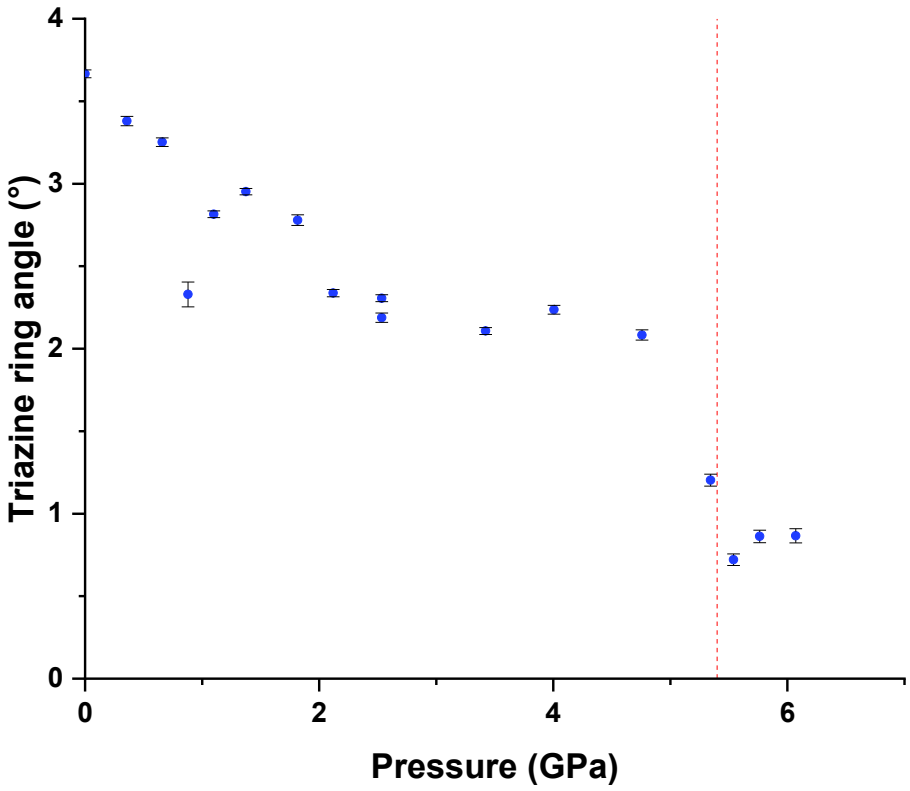

Figure 7 Variation of the "hinge" angle on the triazinyl core (N1-N2-C1-N3∠N1-C3-C2-N3) with increasing pressure.

The sensitivity of the planarity of the triazinyl moiety to the orientations of the phenyl substituents at N1 and C1 was evaluated in a series of DFT calculations using the 6-31G** basis set and the B3LYP exchange-correlation functional. One phenyl group at a time was fixed at intervals of 10° and the geometry of the rest of the molecule allowed to optimise. The results are shown in Figure S6. The torsional angle was also measured on the phenyl substituent that was not fixed during optimisation and the results are shown in the ESI (Figure S7).

The planarity of the triazinyl core is more sensitive to the orientation of the N-Ph than that of the C-Ph substituent, the hinge angle changing by almost 13° as the C3-N1-C14-C19 torsion angle varies between 0 and 180°, becoming essentially planar when the rings are orthogonal. The origin of the effect seems to lie in a relatively short intramolecular H19···H4 interaction which measures 2.026 Å when the rings are coplanar, but 3.393 Å when they are orthogonal (Figure S8). The adoption of a more planar conformation in the triazinyl core at the phase transition thus appears to be a response to the change in the orientation of the N-Ph substituent driven by relief of short intermolecular interactions which build-up at high pressure.

3.6. Volume analysis

Although the discontinuity in the unit cell volume which occurs between 5.34 and 5.54 GPa is indicative of a first order phase transition, the onset of rotation in the N-Ph group and the discontinuities in the intermolecular potentials seen in Figure 4 occur at lower pressure, between 3.42 and 5.34 GPa. Although the changes in Figure 4 are discontinuous, they do not appear to be reflected in other discontinuities in either the unit cell volume or the lattice energy. However, they do represent the onset of new mechanisms for accommodating pressure, and they could be regarded in terms of a premonitory second order phase transition.

The total unit cell volume can be broken down into contributions from interstitial void space and the network of intra- and inter- molecular contacts using the method described in (Novelli *et al.*, 2020, Funnell *et al.*, 2021), where void space corresponds to the regions of the structure lying beyond the van der Waals radius of any of the atoms. Trends in the network and void volumes with pressure can reveal second order effects which are not seen in the overall unit-cell volume.

The variation of the occupied (or 'network') and void volumes with pressure are shown in Figure 8a and b, respectively. Between ambient pressure and 5.34 GPa the network and void volumes decrease by 63.3 (5.8%) and 257.6 (74.7%) Å^3, respectively, indicating that despite the clear changes that occur intra- and inter-molecular geometry, compression is overwhelmingly accommodated by the voids. Accordingly, the network bulk modulus [101(3) GPa] is very much higher than the void bulk modulus [2.2(1) GPa], shown in Table 4, with a similar value to silver or silicon (both 100 GPa) (Gray *et al.*, 2021).

Although the network volume in phase I can be fitted to a single equation of state with a slightly negative curvature, it can also be interpreted in terms of two nearly linear regimes, one between ambient pressure and 2.53 GPa and another between 2.53 and 5.34 GPa (Figure S9). The latter has a steeper gradient as a result of the softening that occurs within the network due to the onset of the new mechanisms for compression, of which rotation of the N-Ph substituent is the most prominent.

Both plots show discontinuities at the phase transition with the network expanding slightly and hardening and the voids softening after the transition, shifting the response even more heavily towards void compression than it had been in phase I.

Table 4 Network volume (V_{net}) and void volume (V_{void}) parameters determined from the EoS fit.

	V_0 (Å^3)	K_0 (GPa)	K_0'	χ^2
V_{tot}	1431.94	7.4(6)	9.3(11)	1.44
V_{net}	1087.00	101(3)	−3(1)	1.56
V_{void}	344.94	2.2(1)	0.8(1)	1.94

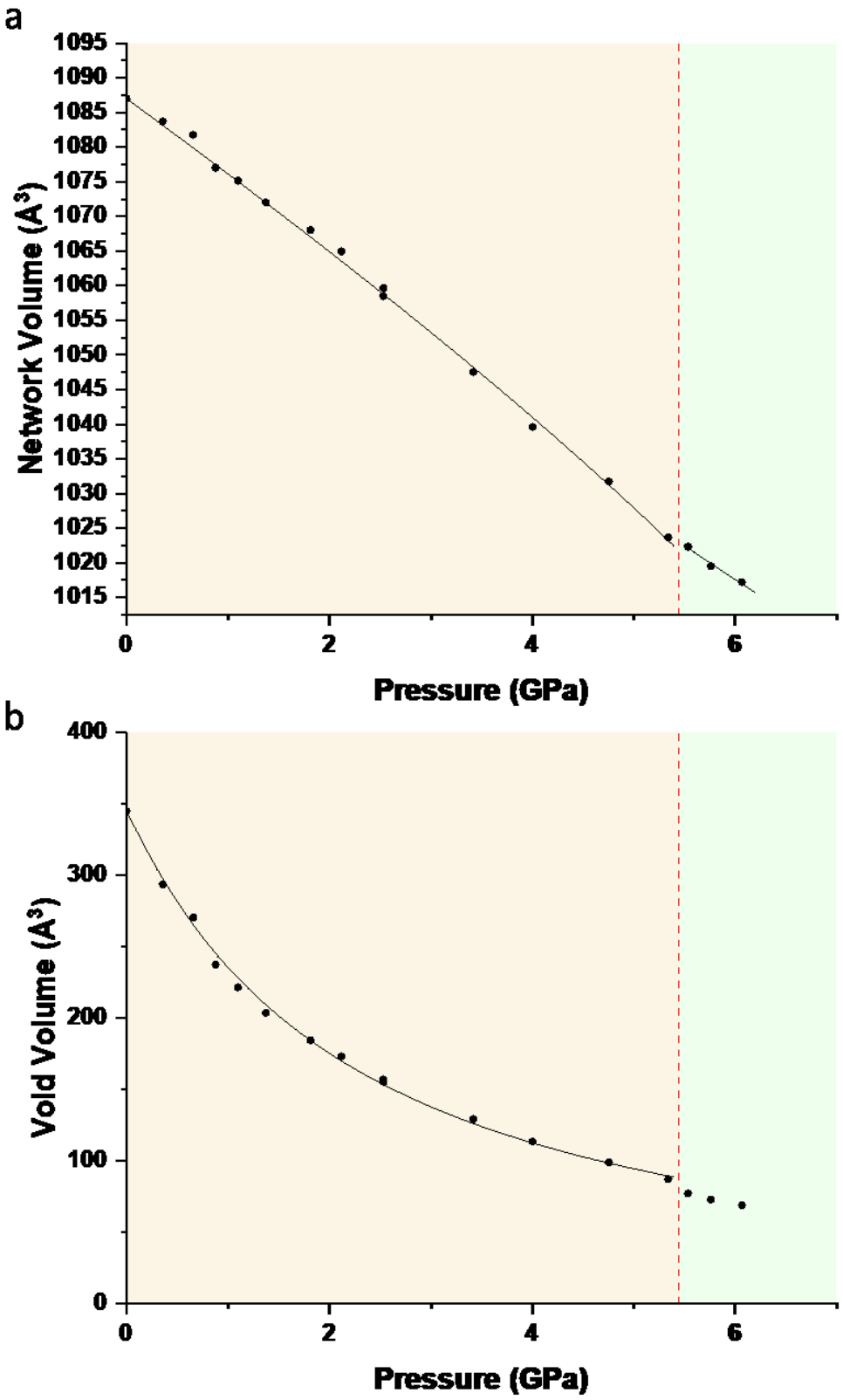

Figure 8 a) Network volume of radical **1** with increasing pressure. The lines show the fit to the 3rd order Birch-Murnaghan equations of state up to 5.34 (Table 4). b) Void volume of **1** with increasing pressure. The line shows the fit to the 3rd order Vinet equation of state up to 5.34 GPa.

3.7. Magneto-structural consequences of the pressure-mediated first order transition

The magnetic properties of Blatter's radical **1** were previously reported by Neugebauer and coworkers (Mukai *et al.*, 1994). At ambient conditions, radical **1** displays typical paramagnetic behaviour as it follows the Curie-Weiss law in the temperature region of 7-300 K with a Curie constant of 0.375 emu K mol^{-1}. Below 7 K antiferromagnetic interactions become dominant with a Weiss constant of −2.2 K. First order phase transition associated with magnetic bistability was previously reported for two Blatter analogues: the 1-phenyl-3-trifluoromethyl-1,4-dihydrobenzo[*e*][1,2,4]triazin-4-yl (Constantinides, Berezin, Zissimou*, et al.*, 2014) and 3-*tert*-butyl-6-cyano-1,4-dihydro-1-phenyl-1,2,4-benzotriazin-4-yl (Takahashi *et al.*, 2018). In both of these radicals, the first order transition takes place in response to temperature as the external stimulus. For the 3-trifluoromethyl analogue the sharp reversible transition occurs at 58(2) K and is fully completed within 5(1) K. This transition proceeds via subtle changes along the 1D π stack. The low temperature phase is diamagnetic with a singlet ground state, stemming from an efficient overlap of the SOMO orbitals and therefore a multicentre two electron interaction. The high-temperature phase is a result of non-interacting S = ½ spins. In the case of Blatter's radical **1**, at ambient conditions the radicals are non-interacting arising from weakly-bound dimers. However, the first order transition that takes place in response to pressure (5.34 GPa) as the external stimuli results in a significant decrease of 0.3-0.4 Å along the stacking direction. It is anticipated that in the resulting high-pressure phase the radicals will experience significant antiferromagnetic interactions due to the decrease of interplanar distances between radicals. This might lead to a diamagnetic singlet ground state. The first order transition triggered by pressure for Blatter's radical **1** could potentially be associated with a spin-transition between a low-pressure paramagnetic state and a high-pressure diamagnetic state.

4. Conclusions

The crystal structure of Blatter's radical **1** has been collected at increasing pressures up to 6.07 GPa. The material exhibited a phase transition in which initial premonitory, and then a discontinuous, rotation of the N-Ph substituent occurred in response to the development of short intermolecular interactions as pressure was increased. The rotation angle of the phenyl substituent influences the planarity of the triazinyl core. Values of the "hinge" angle formed between the triazinyl N1-N2-C1-N3 and N1-C3-C2-N3 moieties in other Blatter derivatives in the Cambridge Structural Database (Groom *et al.*, 2016) are listed in Table S5 of the ESI. The least planar (refcode JUQFEI) is the dimerization product reported by (Berezin *et al.*, 2015). The least planar un-dimerised system is a derivative (CSD refcode DABZEN) with a $-CF_3$ group in the C5 position on the benzo fragment (Constantinides, Koutentis, Krassos*, et al.*, 2011), having a hinge angle of 10.8°. However, the majority of radicals have hinge angles of between 0 and 4°, and so in changing between 3.66° and

planarity, the range of hinge angles seen in radical **1** as a function of pressure spans most of the common range adopted by Blatter derivatives.

The high pressure of the transition in radical **1** currently makes observation of the magnetic response experimentally challenging. Nevertheless, the changes in the conformation of the triazinyl moiety and the compression on the intermolecular π-stacking interactions are likely to have significant consequences for the magnetic properties of **1**, suggesting that the application of high-pressure is a potentially useful method to explore structure-property relationships in organic radicals.

Acknowledgements We thank the University of Edinburgh and the Engineering and Physical Sciences Research Council (UK) for studentship funding awarded to E.T.B. and C.J.G.W. (grant no. EP-M506515-1) and for provision of equipment (Grant EP/R042845/1), and the Cambridge Crystallographic Data Centre for studentship funding to C.J.G.W. C.P.C. thanks the University of Michigan–Dearborn for a UM-Dearborn Scholars award. P.A.K. thanks the Cyprus Research Promotion Foundation and the following organizations and companies in Cyprus for generous donations of chemicals and glassware: the State Laboratory, the Agricultural Research Institute, the Ministry of Agriculture, MedoChemie Ltd., Medisell Ltd., Biotronics Ltd. and the A. G. Leventis Foundation for helping to establish the NMR facility at the University of Cyprus.

References

Alvarez, S. (2013). *Dalton Trans.* **42**, 8617-8636.
Angel, R. J., Alvaro, M. & Gonzalez-Platas, J. (2014). *Z. Kristallogr. - Cryst. Mater.* **229**, 405-419.
Bartos, P., Young Jr, V. G. & Kaszynski, P. (2020). *Org. Lett.* **22**, 3835-3840.
Berezin, A. A., Constantinides, C. P., Drouza, C., Manoli, M. & Koutentis, P. A. (2012). *Org. Lett.* **14**, 5586-5589.
Berezin, A. A., Constantinides, C. P., Mirallai, S. I., Manoli, M., Cao, L. L., Rawson, J. M. & Koutentis, P. A. (2013). *Org. Biomol. Chem.* **11**, 6780-6795.
Berezin, A. A., Zissimou, G., Constantinides, C. P., Beldjoudi, Y., Rawson, J. M. & Koutentis, P. A. (2015). *J. Org. Chem.* **80**, 8943-8944.
Blatter, H. M. & Lukaszewski, H. (1968). *Tetrahedron Lett.* **9**, 2701-2705.
Bruker (2019). *APEX3* Version 2019.11-0. Bruker AXS Inc., Madison, Wisconsin.
Cliffe, M. J. & Goodwin, A. L. (2012). *J. Appl. Cryst.* **45**, 1321-1329.
Constantinides, C. P., Berezin, A. A., Manoli, M., Leitus, G. M., Zissimou, G. A., Bendikov, M., Rawson, J. M. & Koutentis, P. A. (2014). *Chem. Eur. J.* **20**, 5388-5396.
Constantinides, C. P., Berezin, A. A., Zissimou, G. A., Manoli, M., Leitus, G. M., Bendikov, M., Probert, M. R., Rawson, J. M. & Koutentis, P. A. (2014). *J. Am. Chem. Soc.* **136**, 11906-11909.
Constantinides, C. P. & Koutentis, P. A. (2016). *Adv. Heterocycl. Chem.* **119**, 173-207.
Constantinides, C. P., Koutentis, P. A., Krassos, H., Rawson, J. M. & Tasiopoulos, A. J. (2011). *J. Org. Chem.* **76**, 2798-2806.
Constantinides, C. P., Koutentis, P. A. & Loizou, G. (2011). *Org. Biomol. Chem.* **9**, 3122-3125.
Constantinides, C. P., Lawson, D. B., Zissimou, G. A., Berezin, A. A., Mailman, A., Manoli, M., Kourtellaris, A., Leitus, G. M., Clérac, R. & Tuononen, H. M. (2020). *CrystEngComm* **22**, 5453-5463.
Cruz-Cabeza, A. J., Davey, R. J., Oswald, I. D. H., Ward, M. R. & Sugden, I. J. (2019). *CrystEngComm* **21**, 2034-2042.
Dawson, A., Allan, D. R., Parsons, S. & Ruf, M. (2004). *J. Appl. Cryst.* **37**, 410-416.

Dolomanov, O. V., Bourhis, L. J., Gildea, R. J., Howard, J. A. K. & Puschmann, H. (2009). *J. Appl. Cryst.* **42**, 339-341.
Etcheverry-Berrios, A., Parsons, S., Kamenev, K. V., Probert, M. R., Moggach, S. A., Murrie, M. & Brechin, E. K. (2020). *Magnetochemistry* **6**, 32.
Frisch, M. J., Trucks, G. W., Schlegel, H. B., Scuseria, G. E., Robb, M. A., Cheeseman, J. R., Scalmani, G., Barone, V., Mennucci, B., Petersson, G. A., Nakatsuji, H., Caricato, M., Li, X., Hratchian, H. P., Izmaylov, A. F., Bloino, J., Zheng, G., Sonnenberg, J. L., Hada, M., Ehara, M., Toyota, K., Fukuda, R., Hasegawa, J., Ishida, M., Nakajima, T., Honda, Y., Kitao, O., Nakai, H., Vreven, T., Montgomery Jr., J. A., Peralta, J. E., Ogliaro, F., Bearpark, M., Heyd, J. J., Brothers, E., Kudin, K. N., Staroverov, V. N., Kobayashi, R., Normand, J., Raghavachari, K., Rendell, A., Burant, J. C., Iyengar, S. S., Tomasi, J., Cossi, M., Rega, N., Millam, J. M., Klene, M., Knox, J. E., Cross, J. B., Bakken, V., Adamo, C., Jaramillo, J., Gomperts, R., Stratmann, R. E., Yazyev, O., Austin, A. J., Cammi, R., Pomelli, C., Ochterski, J. W., Martin, R. L., Morokuma, K., Zakrzewski, V. G., Voth, G. A., Salvador, P., Dannenberg, J. J., Dapprich, S., Daniels, A. D., Farkas, Ö., Foresman, J. B., Ortiz, J. V., Cioslowski, J. & Fox, D. J. (2009). *Gaussian 09 , Revision B.01, Gasussian, Inc.*
Funnell, N. P., Allan, D. R., Maloney, A. G. P., Smith, R. I., Wilson, C. J. G. & Parsons, S. (2021). *CrystEngComm* **23**, 769-776.
Funnell, N. P., Bull, C. L., Ridley, C. J. & Capelli, S. (2019). *CrystEngComm* **21**, 4473-4483.
Gallagher, N. M., Bauer, J. J., Pink, M., Rajca, S. & Rajca, A. (2016). *J. Am. Chem. Soc.* **138**, 9377-9380.
Gaspar, A. B., Molnár, G., Rotaru, A. & Shepherd, H. J. (2018). *C. R. Chim.* **21**, 1095-1120.
Gavezzotti, A. (2005). *Z. Kristallogr. - Cryst. Mater.* **220**, 499-510.
Gavezzotti, A. (2007). *Molecular aggregation: structure analysis and molecular simulation of crystals and liquids*. OUP Oxford.
Gavezzotti, A. (2011). *New J. Chem.* **35**, 1360-1368.
Giordano, N., Afanasjevs, S., Beavers, C. M., Hobday, C. L., Kamenev, K. V., O'Bannon, E. F., Ruiz-Fuertes, J., Teat, S. J., Valiente, R. & Parsons, S. (2019). *Molecules* **24**, 2018.
Gray, T., Whitby, M. & Mann, N. (2021). *Bulk Modulus for All the Elements in the Periodic Table,* https://periodictable.com/Properties/A/BulkModulus.html.
Groom, C. R., Bruno, I. J., Lightfoot, M. P. & Ward, S. C. (2016). *Acta Cryst.* **B72**, 171-179.
Guionneau, P. & Collet, E. (2013). *Spin-Crossover Materials*, pp. 507-526.
Halcrow, M. A. (2007). *Polyhedron* **26**, 3523-3576.
Hande, A. A., Darrigan, C., Bartos, P., Baylère, P., Pietrzak, A., Kaszyński, P. & Chrostowska, A. (2020). *PCCP* **22**, 23637-23644.
Ji, Y., Long, L. & Zheng, Y. (2020). *Mater. Chem. Front.* **4**, 3433-3443.
Johnstone, R. D. L., Lennie, A. R., Parker, S. F., Parsons, S., Pidcock, E., Richardson, P. R., Warren, J. E. & Wood, P. A. (2010). *CrystEngComm* **12**, 1065-1078.
Kaszyński, P., Constantinides, C. P. & Young Jr, V. G. (2016). *Angew. Chem. Int. Ed.* **55**, 11149 – 11152
Katrusiak, A. (2019). *Acta Cryst.* **B75**, 918-926.
Klotz, S., Chervin, J. C., Munsch, P. & Le Marchand, G. (2009). *J. Phys. D* **42**, 075413.
Koutentis, P. A. & Lo Re, D. (2010). *Synthesis* **2010**, 2075-2079.
Leitch, A. A., Lekin, K., Winter, S. M., Downie, L. E., Tsuruda, H., Tse, J. S., Mito, M., Desgreniers, S., Dube, P. A. & Zhang, S. (2011). *J. Am. Chem. Soc.* **133**, 6051-6060.
Mackenzie, C. F., Spackman, P. R., Jayatilaka, D. & Spackman, M. A. (2017). *IUCrJ* **4**, 575-587.
Macrae, C. F., Sovago, I., Cottrell, S. J., Galek, P. T. A., McCabe, P., Pidcock, E., Platings, M., Shields, G. P., Stevens, J. S., Towler, M. & Wood, P. A. (2020). *J. Appl. Cryst.* **53**, 226-235.
Mailman, A., Leitch, A. A., Yong, W., Steven, E., Winter, S. M., Claridge, R. C. M., Assoud, A., Tse, J. S., Desgreniers, S. & Secco, R. A. (2017). *J. Am. Chem. Soc.* **139**, 2180-2183.
Mao, H. K., Bell, P. M., Shaner, J. W. t. & Steinberg, D. J. (1978). *J. Appl. Phys.* **49**, 3276-3283.
McKellar, S. C. & Moggach, S. A. (2015). *Acta Cryst.* **B71**, 587-607.
Merrill, L. & Bassett, W. A. (1974). *Rev. Sci. Inst.* **45**, 290-294.
Moggach, S. A., Allan, D. R., Clark, S. J., Gutmann, M. J., Parsons, S., Pulham, C. R. & Sawyer, L. (2006). *Acta Cryst.* **B62**, 296-309.

Moggach, S. A. & Oswald, I. D. H. (2020). *21st Century Challenges in Chemical Crystallography I: History and Technical Developments*, edited by D. M. P. Mingos & P. R. Raithby, pp. 141-198. Cham: Springer International Publishing.
Mukai, K., Inoue, K., Achiwa, N., Jamali, J. B., Krieger, C. & Neugebauer, F. A. (1994). *Chem. Phys. Lett.* **224**, 569-575.
Novelli, G., Maynard-Casely, H. E., McIntyre, G. J., Warren, M. R. & Parsons, S. (2020). *Crystal Growth & Design* **20**, 7788-7804.
Reeves, M. G., Wood, P. A. & Parsons, S. (2020). *J. Appl. Cryst.* **53**, 1154-1162.
Rogers, F. J. M., Norcott, P. L. & Coote, M. L. (2020). *Org. Biomol. Chem.* **18**, 8255-8277.
Savva, A. C., Mirallai, S. I., Zissimou, G. A., Berezin, A. A., Demetriades, M., Kourtellaris, A., Constantinides, C. P., Nicolaides, C., Trypiniotis, T. & Koutentis, P. A. (2017). *J. Org. Chem.* **82**, 7564-7575.
Sheldrick, G. M. (2015). *Acta Cryst.* **A71**, 3-8.
Sinnokrot, M. O., Valeev, E. F. & Sherrill, C. D. (2002). *J. Am. Chem. Soc.* **124**, 10887-10893.
Spackman, M. A., McKinnon, J. J. & Jayatilaka, D. (2008). *CrystEngComm* **10**, 377-388.
Spackman, P. R., Turner, M. J., McKinnon, J. J., Wolff, S. K., Grimwood, D. J., Jayatilaka, D. & Spackman, M. A. (2021). *J. Appl. Cryst.* **54**.
Takahashi, Y., Tsuchiya, N., Miura, Y. & Yoshioka, N. (2018). *New J. Chem.* **42**, 9949-9955.
Thorn, A., Dittrich, B. & Sheldrick, G. M. (2012). *Acta Cryst.* **A68**, 448-451.
Turner, M. J., Thomas, S. P., Shi, M. W., Jayatilaka, D. & Spackman, M. A. (2015). *Chem. Commun.* **51**, 3735-3738.
Wilson, C. J. G., Cervenka, T., Wood, P. A. & Parsons, S. (2021). *Manuscript in preparation*.
Wood, P. A., Francis, D., Marshall, W. G., Moggach, S. A., Parsons, S., Pidcock, E. & Rohl, A. L. (2008). *CrystEngComm* **10**, 1154-1166.
Zakharov, B. A. & Boldyreva, E. V. (2019). *CrystEngComm* **21**, 10-22.